Revue des Energies Renouvelables Vol. 22 N°1 (2019) 19 - 35
DOI: https://doi.org/10.54966/jreen.v22i1.722

Numerical investigation of coaxial turbulent jet

Nabil Belkacem Safer * and Abdelhadi Beghidja

Laboratory of Renewable Energies and Sustainable Development,
Department of Mechanical Engineering,
University 1, Constantine, Algeria

(reçu le 10 Mars 2019 - accepté le 25 Mars 2019)

Résumé – *Ce travail présente une étude numérique de jet coaxial compressible et turbulent par simulation des grandes échelles. En considérant la configuration de jet coaxial avec un jet primaire chaud et un jet secondaire non chauffé. La démarche de recherche de ce travail s'est articulée sur la mise en œuvre d'une méthode numérique performante et moderne en permettant de répondre aux exigences en termes de précision des résultats et coût de calcul. Un nouveau solveur de linéarisation des équations caractéristiques du problème Riemann est utilisé dans ce travail. Cette étude est portée sur la compréhension du scénario de transition des jets coaxiaux vers la turbulence en focalisant sur la dynamique tourbillonnaire de ces écoulements. Cette étude a abouti que la première étape de transition à la turbulence de jet coaxial est initiée par le développement d'instabilités de Helmholtz (structures primaires) au niveau des couches cisaillées. Alors que La seconde étape est initie réellement la tridimensionnalisation du jet coaxial, et l'appariement fractionnel des structures tourbillonnaires secondaires. L'évolution transversale des tenseurs de Reynolds ont montré que la contribution du tenseur de Reynolds axiale est associée à l'instabilité primaire, alors que la contribution du tenseur de Reynolds transversal est associé à l'instabilité secondaire. L'état de l'autosimilarité est obtenu dans la région de turbulence pleinement développé. La prédominance du mode axisymétrique sur chacune des couches de cisaillées dans la région initiale de l'écoulement. Les résultats obtenus ont un bon accord avec les résultats expérimentaux similaire à notre jet simulé.*

Abstract – *The paper presents a numerical study of a compressible and turbulent coaxial jet, using a Large Eddy Simulation type approach. This study focuses on the implementation of a high-performance and modern numerical method to meet the requirements in terms of results accuracy and calculation cost. The code was parallelized using the Message Passing Interface 'MPI' library. Inviscid fluxes are evaluated using a new linearization solver for the equations characteristic of approximate Riemann problem and the solution has been advanced over time using an explicit two-step McCormack method. The purpose of this study is to understand the initial stage of the transition process from laminar to turbulent flow in coaxial jets. Therefore, it has been determined that the first step in the transition process from laminar to turbulent flow in coaxial jets is initiated by the development of Helmholtz (primary vortices) in sheer layers, while three-dimensionalization turbulence is initiated in the second step with the emergence of secondary vortices. The transverse evolution of Reynolds tensors showed that the axial Reynolds tensor contribution is associated with primary instability while the transversal Reynolds tensor contribution is associated with secondary instability. Flow self-similarity state is obtained in fully developed turbulence region. Axi-symmetric mode predominates on each shear layer in the initial flow region. The results obtained are in good agreement with experimental results similar to this study's simulated jet*.

Keywords: Coaxial jet - Riemann solver - Muscl.

1. INTRODUCTION

Coaxial jets are considered an effective way to mix two different fluids. Coaxial jet configuration is widely used in industrial systems, such as combustion chambers and

* safer_n@hotmail.com

gas turbines. Achieving a better mixture improves combustion efficiency and reduces pollutant emissions into the atmosphere. Mixing properties in coaxial jets are regulated by the development of structures from internal and external shear zones and their interactions after the junction point. Few research works have studied coaxial jet flows.

Champagne *et al.* [1] have concluded that most of the mixing process takes place in the jet development region at the potential cones. In addition, Warda *et al.* [2] have noted that coaxial jets, with a velocity ratio starting at more than one unit, developed faster than jets with a velocity ratio below one unit.

Forstall *et al.* [3] have been the first to study the effect of different input velocity ratios on the mixture. They have concluded that the velocity ratio is a very important and determining parameter on the quality of the mixture.

Ko *et al.* [4, 5] have divided the development of coaxial jets into three zones: initial development zone, intermediate zone, and a fully developed zone. The initial development zone extends from the beginning of the jet to the end of the external potential cone and the fully developed zone refers to the point where the two jets have completely fused and therefore the coaxial jet operates as a single jet.

Intermediate zone is the area between the initial development region and fully developed region. The main parameter determining the properties of compressible coaxial jets is the mean flow velocity ratio. Buresti *et al.* [6] have studied the flow properties in the near-field of coaxial jets.

S.C. Crow *et al.* [6] have studied the role of coherent vortices in the mixing process, since large scale, coherent vortices induced by sheared flows play an important role in turbulent transport. Villermaux *et al.* [8] have shown that the concentration field of a passive tracer injected into the jet has an evolution and characteristic quantities correlated to the velocity field. They have determined the mixing time scale according to Schmidt's number. Rehab *et al.* [9] have studied the distribution of a passive tracer within a coaxial flow. Ferrao *et al.* [10] have shown that the mixing at the inner jet was influenced by the outer sheared layer dynamics. Recirculation zone impact on mixing properties is significant.

Several numerical studies have been performed to understand the flow and scalar mixing in coaxial jets. For example, Da Silva *et al.* [11] have performed a (DNS) of a coaxial jet, and Da Silva *et al.* [12] have studied the transition to turbulence at very high-velocity ratios. Balarac *et al.* [13] have also studied the near-field of coaxial jets, and subsequently analyzed the influence of the internal shear layer on momentum thickness. Balarac *et al.* [14] have simulated coaxial jets with high-velocity ratios under different input conditions, while Dianat *et al.* [15] have performed an (LES) simulation of the mixing passive scalar.

Jahnke *et al.* [16] have conducted a simulation (LES) of mixing in a confined coaxial jet. They have studied the influence of different parameters such as the Reynolds number, Schmidt number, and density ratio, and have considered the case where the internal jet is faster than the external jet. More recent numerical studies have been conducted by Balarac *et al.* [17], Dinesh *et al.* [18], Michael Reto Gloor [19].

This study aims to accurately characterize the transition process from laminar to turbulent flow in a coaxial jet. Therefore, the paper presents a numerical study of the compressible and turbulent coaxial jet using a Large Eddy Simulation.

This study focuses on the implementation of a high-performance and modern numerical method to meet the requirements in terms of results accuracy and calculation cost. A new linearization solver for the equations characteristic of the approximate Riemann problem was used to calculate inviscid flux.

In addition, a three-dimensional compressible parallel finite-volume code for the coaxial jet was developed. The Message Passing Interface (MPI) library was also used in this work.

The remainder of the article is organized as follows: Section 2 presents the dimensionless governing equations for compressible coaxial jet flow. Section 3 describes the method of resolution used in this study, while Section 4 discusses the results. Finally, Section 4 summarises the results of this work and draws conclusions.

2. GOVERNING EQUATIONS

The filtered and dimensioned equations for conservation of mass, momentum, and energy, under the conservative form, are expressed as follows:

$$\frac{\partial U}{\partial t} + \frac{\partial F}{\partial x} + \frac{\partial G}{\partial y} + \frac{\partial H}{\partial z} = 0 \tag{1}$$

Where, U is the vector of the conservative variables; and F, G, and H represent the numerical flows on each flow direction x, y, and z.

Where,

$$U \begin{bmatrix} \rho \\ \rho u \\ \rho v \\ \rho w \\ \rho e \end{bmatrix}$$

Where ρ, u, v, v, and e are the density, the axial, transverse velocity components in y and z and the total interne energy, respectively. System (1) is completed by the definition of total interne energy for a perfect gas:

$$\rho e = \frac{p}{\gamma - 1} + \frac{1}{2}\rho(u^2 + v^2 + w^2) \tag{2}$$

Equations systems are closed using state equation for a perfect gas:

$$P = \rho R T \tag{3}$$

Spatial derivatives of fluxes in {Eq. (1)} for Cartesian grid can be expressed by spatial finite differencing operators that retain conservation property:

$$L_h(\overline{U}^n_{ijk}) = \frac{F^n_{i-\frac{1}{2},j,k} - F^n_{i+\frac{1}{2},j,k}}{\Delta x} + \frac{G^n_{i,j-\frac{1}{2},k} - G^n_{i,j+\frac{1}{2},k}}{\Delta y} + \frac{H^n_{i,j,k-\frac{1}{2}} - F^n_{i,j,k+\frac{1}{2}}}{\Delta z} \tag{4}$$

In order to compute the numerical fluxes F, G, and H in {Eq. (1)}, the fluxes were split into viscous fluxes: F_{vis}, G_{vis}, and H_{vis}, and inviscid fluxes F_{inv}, G_{inv}, and H_{inv}.

$$F_{inv}\begin{bmatrix} \rho u \\ p+\rho u^2 \\ \rho u v \\ \rho u w \\ (\rho e+p)u \end{bmatrix} \quad G_{inv}\begin{bmatrix} \rho v \\ \rho u v \\ p+\rho v^2 \\ \rho v w \\ (\rho e+p)v \end{bmatrix} \quad H_{inv}\begin{bmatrix} \rho w \\ \rho w u \\ \rho w v \\ p+\rho w^2 \\ (\rho e+p)w \end{bmatrix}$$

$$F_{vis}\begin{bmatrix} 0 \\ (1/\mathrm{Re}+\mu_t/\mu)\,\tau_{l1} \\ (1/\mathrm{Re}+\mu_t/\mu)\,\tau_{l2} \\ (1/\mathrm{Re}+\mu_t/\mu)\,\tau_{l3} \\ \left(\frac{\mu}{\alpha}+\frac{\mu_t}{\alpha_t}\right)\frac{\partial T}{\partial x}+\frac{1}{\mathrm{Re}}\left(u\tau_{l1}+v\tau_{l2}+w\tau_{l3}\right) \end{bmatrix}$$

$$G_{vis}\begin{bmatrix} 0 \\ (1/\mathrm{Re}+\mu_t/\mu)\,\tau_{21} \\ (1/\mathrm{Re}+\mu_t/\mu)\,\tau_{22} \\ (1/\mathrm{Re}+\mu_t/\mu)\,\tau_{23} \\ \left(\frac{\mu}{\alpha}+\frac{\mu_t}{\alpha_t}\right)\frac{\partial T}{\partial y}+\frac{1}{\mathrm{Re}}\left(u\tau_{21}+v\tau_{22}+w\tau_{23}\right) \end{bmatrix}$$

$$H_{vis}\begin{bmatrix} 0 \\ (1/\mathrm{Re}+\mu_t/\mu)\,\tau_{31} \\ (1/\mathrm{Re}+\mu_t/\mu)\,\tau_{32} \\ (1/\mathrm{Re}+\mu_t/\mu)\,\tau_{33} \\ \left(\frac{\mu}{\alpha}+\frac{\mu_t}{\alpha_t}\right)\frac{\partial T}{\partial z}+\frac{1}{\mathrm{Re}}\left(u\tau_{31}+v\tau_{32}+w\tau_{33}\right) \end{bmatrix}$$

Where:

$$\alpha=\frac{\gamma-1}{M^2.\mathrm{Re}.\mathrm{Pr}},\quad \alpha_t=(\gamma-1)M^2\,\mathrm{Pr}_t,\quad \gamma=C_V/C_P$$

Re: Reynolds number flow; Pr: Prandtl number; Pr_t: Turbulent Prandtl number; M: Mach number; γ: Heat capacity ratio.

The viscous stress tensor τ_{ij} is defined by:

$$\tau_{ij}=\frac{1}{2}\left(\frac{\partial u_i}{\partial x_j}+\frac{\partial u_j}{\partial x_i}-\frac{2}{3}\delta_{ij}\left(\frac{\partial u_k}{\partial x_k}\right)\right) \tag{5}$$

2.1 Turbulence model

LES is an alternative for computing flows at higher Reynolds number. In this technique, only the larger structures are computed, and the effects of smaller scales are taken into account via a sub-grid scale model. A turbulent viscosity μ_t ensures dissipation of the smaller unresolved structures. Various models have been built to determine an expression of this turbulent viscosity. In order to simplify the problem as much as possible from an aerodynamic point of view, we chose the Smagorinsky model:

$$\mu_t=\rho(C_s\Delta)^2\sqrt{2S_{ij}S_{ij}} \tag{6}$$

Where C_s is a Smagorinsky [20] model parameter, and Δ is the filter width and is defined:

$$\Delta = (\Delta_x \Delta_y \Delta_z)^{1/3} \tag{7}$$

Where Δ_x, Δ_y, Δ_z are the local mesh spacing in x, y and z directions respectively.

S_{ij} is the stress tensor given by:

$$S_{ij} = \frac{1}{2}\left(\frac{\partial u_i}{\partial x_j} + \frac{\partial u_j}{\partial x_i} \right) \tag{8}$$

2.2 Initial condition

Similar to a single jet initial profile, an initial hyperbolic double tangent velocity profile is used to approximate the actual velocity profile of a coaxial jet, as follows:

$$u(r) = \begin{cases} U_S - \dfrac{U_P - U_S}{2}\left(1 - \tanh\left(\dfrac{R_p}{4\theta_P}\left(\dfrac{r}{R_P} - \dfrac{R_P}{r}\right)\right)\right) \text{ if } \quad r \le R_m \\ U_\infty - \dfrac{U_S - U_\infty}{2}\left(1 - \tanh\left(\dfrac{R_S}{4\theta_S}\left(\dfrac{r}{R_S} - \dfrac{R_S}{r}\right)\right)\right) \text{ if } \quad r > R_m \end{cases} \tag{9}$$

The pattern is defined using the momentum thickness of the shear layer θ_P and θ_S of primary and secondary jet respectively.

Similar to single jets, the temperature distribution is given by Crocco-Busemann relation:

$$\frac{T}{T_p}(r) = \frac{T_\infty}{T_p} + \left(1 - \frac{T_\infty}{T_p}\right)\frac{U}{U_p}(r) + \frac{\gamma - 1}{2} M^2 \frac{U}{U_p}(r)\left(1 - \frac{U}{U_p}(r)\right) \tag{10}$$

2.3 Boundary conditions

White noise is overlaid on the initial input velocity profile to trigger jet disruption and development of Kelvin-Helmholtz Instabilities in internal and external shear layers based on instability linear theory. This noise has a small amplitude of about 3 % of the input velocity.

Velocity components in transverse direction y and z are zero. Randomly generated disturbances are imposed on the transverse direction y and z. Upper and lower boundaries of the sliding conditions calculation range were prescribed. Front and rear boundaries of the domain are periodic and boundary conditions at the exit of the domain are convective. Figure 1 illustrates the boundary conditions of the simulation.

3. NUMERICAL TOOLS

To calculate viscous components of numerical flux, viscous flows are computed from the second-order central difference in space. In addition, to evaluate inviscid fluxes on cell boundaries, it is, therefore, necessary to evaluate inviscid fluxes by solving a multidimensional Euler problem using a new linearization solver for the characteristic equations of the approximate Riemann problem. The approximate three-dimensional Riemann solver is described in the following steps.

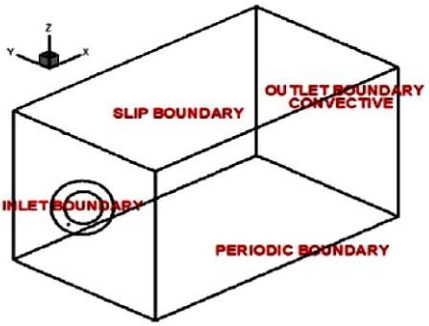

Fig. 1: Boundary condition

In the first step, the flux vector F_{inv} is evaluated with u as the normal velocity component, and v and w as the tangential components, the tangential components are passively convected by the normal component, but by taking the direction of the flow of information in the normal direction into consideration.

Similarly, the flux vector G_{inv} is evaluated using v as the normal velocity component, and u and w as the tangential components.

Finally, the flux vector H_{inv} is evaluated using w as the normal velocity component, and u and v as the tangential components (Kopchenov *et al.*) [22].

The conservative variable values on the left and right of the interface $(i+1/2)$ are calculated using the third order Muscl scheme [23] as follows:

$$U^n_{i+1/2,L} = U^n_i + \frac{1-\varphi}{4}\Delta\overline{W}^n_{i+1/2} + \frac{1+\varphi}{4}\Delta\overline{W}^n_{i-1/2} \quad (11)$$

$$U^n_{i+1/2,R} = U^n_{i+1} + \frac{1+\varphi}{4}\Delta\overline{W}^n_{i-1/2} + \frac{1-\varphi}{4}\Delta\overline{W}^n_{i+1/2} \quad (12)$$

$$\Delta W^n_{i+1/2} = W^n_{i+1} - W^n_i \quad (13)$$

$$\Delta W^n_{i61/2} = W^n_i - W^n_{i-1} \quad (14)$$

$$\Delta\overline{W}^n_{i+1/2} = \min\mathrm{mod}(\Delta W^n_{i-1/2}, B\times\Delta W^n_{i+1/2}) \quad (15)$$

$$\Delta\overline{W}^n_{i-1/2} = \min\mathrm{mod}(\Delta W^n_{i+1/2}, B\times\Delta W^n_{i-1/2}) \quad (16)$$

The minmod flux limiter is defined as:

$$1 \le B \le \frac{(3-\varphi)}{(1-\varphi)} \quad (17)$$

$$\mathrm{minimode}[x,y] = \mathrm{sign}(x)\times\max\left[0,\min\left(|x|, y\times\mathrm{sign}(x)\right)\right] \quad (18)$$

$$W = [\rho, u, v, w, p] \quad (19)$$

The solution was advanced over time using a two-stage explicit McCormack [24]. This method is accurate, efficient and simple to implement on parallel computers.

The time step is determined by the stability analysis of a numerical scheme, which verifies the Friedrichs-Lewy Current criterion and is defined by a classical advective criterion Δt_1, and a diffusive criterion Δt_2:

$$\Delta t_1 = \frac{CFL}{\max\left(\frac{|u|+c}{\Delta x}, \frac{|v|+c}{\Delta x}, \frac{|w|+c}{\Delta x}\right)} \quad (20)$$

$$\Delta t_2 = \frac{CFL}{\max\left(\frac{4\mu}{3\rho}, \frac{\gamma.\mu}{\rho;Pr}\right)\left(\frac{1}{\Delta x^2}, \frac{1}{\Delta y^2}, \frac{1}{\Delta z^2}\right)} \quad (21)$$

$$\Delta t = \min(\Delta t_1, \Delta t_2) \quad (22)$$

4. RESULTS AND DISCUSSION

Calculation range extends over $30D_p$ in the axial direction and $17D_p$ in the transverse directions y and z.

$$\lfloor L_x \times L_y \times L_z \rfloor = \lfloor 30D_p \times 17D_p \times 17D_p \rfloor$$

The main physical characteristics of the simulated jet are given in **Table 1**.

Table 1: Physical parameters of coaxial jet simulations

U_s/U_p	D_p/D_s	T_p/T_s	M_p	M_s	Re_p	U_s/U_{amb}	T_s/T_{amb}
0.7	2	2.7	0.5	0.57	$6.2.10^{-5}$	0.1	1

Fluctuation component of the flow variables (velocity and mixture fraction) is calculated based on the instantaneous variable mean obtained with (LES) over a total time equal to 10 times the time for the input flow velocity to reach the output boundary. This will allow the flow field to fully develop and any initial transition will leave the computation domain

$$\langle \tilde{f} \rangle = \frac{1}{N_t} \sum_{n=1}^{N_t} \tilde{f}^n \quad (23)$$

$$\tilde{f}_{rms} = \sqrt{\frac{1}{N_t} \sum_{n=1}^{N_t} (\tilde{f}^n - \langle \tilde{f} \rangle)^2} \quad (24)$$

Where, N_t is the number of step time.

4.1 Mesh size selection

Three Cartesian structured meshes with different mesh densities (3D) were tested to study the mesh sensitivity, when the mesh resolution is sufficiently improved.

Table 2: Different mesh simulations

Mesh 1	**Mesh 2**	**Mesh 3**
160x75x75	215x125x125	385x125x125

Figure 2 shows the development of the longitudinal velocity fluctuation speof the longiyuctrum of the primary jet axis i fluctuation $x/D_p = 10$. Figure 2 shows that the solder used in this work properly detects turbulence when the resolution of the mesh is sufficiently improve.

The spectrum has an inertial zone with a power law in $K = -5/3$. This observation indicates that large eddies are well represented with minimal dependence on short waves as the calculation mesh increases.

Therefore, this result shows that the solver used is chosen for its stability, convergence robustness and high degree of validation. The mesh used in the rest of the work will be 385 x 125 x 125 points. This choice is based on the compromise between the available computing materials and the accuracy of the results.

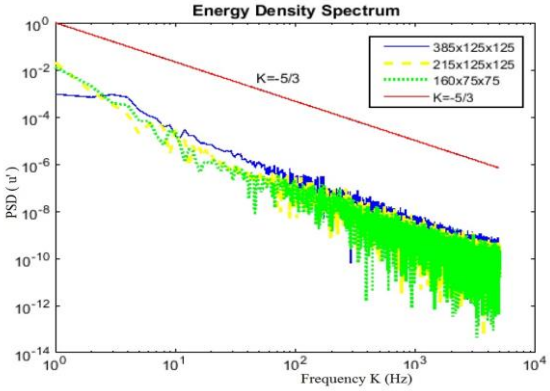

Fig. 2: PSD longitudinal velocity at different grid resolutions

4.2 Validation

Figure 3 shows the evolution of the fluctuation rate of axial velocity on the primary jet axis. The hot jet reaches its maximum amplitude of turbulent intensity on the primary jet axis, in accordance with the position of the potential cone.

Growth in turbulence intensity on the primary jet axis is increased up to $x/D_p = 5$, and peak amplitude of turbulent intensity is reached when internal and external shear layers merge. Therefore, these results agree with Guitton *et al.* [25] experimental data.

Figure 4 illustrates the decrease in longitudinal velocity along the primary jet axis of each simulation. Potential cone length is defined to reduce the average longitudinal velocity to 95 % of the jet inlet velocity at $y = 0$.

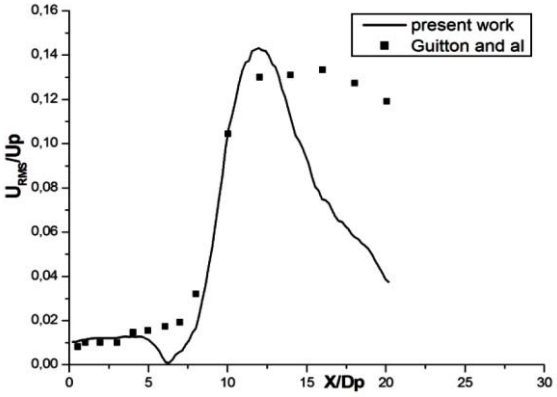

Fig. 3: RMS axial velocity profile in axial direction

According to figure 4, the potential cone of the primary jet is $x/D_p = 7.5$. On the other hand, the behavior of the decrease in velocity profile is similar to that obtained by the experimental results [25]. As a result, due to the Cartesian approach, the dissipative nature of this numerical scheme and sub grid model turbulence.

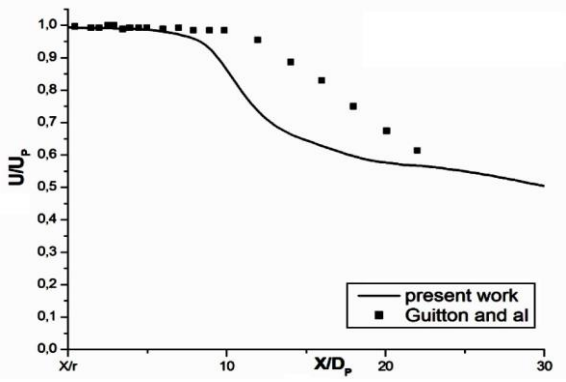

Fig. 4: The decay of the longitudinal velocity along the coaxial jet axis

Figure 5 shows the average contour of longitudinal velocity in the vertical symmetry plane of the jet.

Figure 5 also indicates that at the beginning of the jet, the longitudinal velocities at the center of the internal and external jet ($y/D_p = 0$ and $x/D_p = 7.5$, respectively) are maintained along potential cones (internal and external).

Beyond $x/D_p = 10$ there is a high transverse transfer of momentum quantity, and velocity profile becomes a similar evolution to a transverse profile of a single jet.

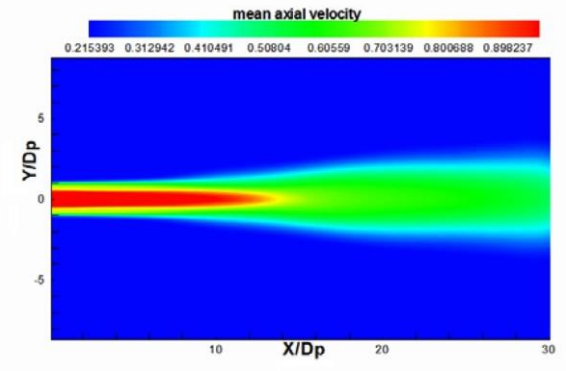

Fig. 5: Cut through the plane (x, y) of the mean fields of the longitudinal velocity

Figure 6 represents the contour of the instantaneous longitudinal velocity in the vertical symmetry plane of the jet. Therefore, four shear zones develop in mixing layers in the vertical plane as soon as they exit jet. While two shear zones occur at the secondary jet and ambient environment interface and two others develop at the primary and secondary jet interface.

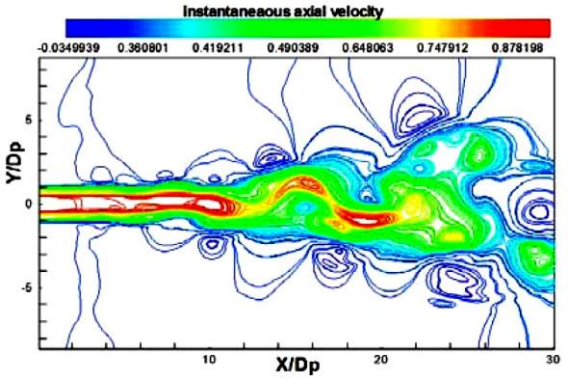

Fig. 6: Cut through the plane (x, y) of the instantaneous fields of the longitudinal velocity

Figure 7 presents a cross-section through the plane (*x*, *y*) of the vorticity field. Similar to round jets, the transition is initiated by the development of Kelvin Helmholtz instabilities in shear layers, which are the result of ring-forming vortices.

These rings are located either between internal and external jet (these are the internal primary vortices) or between the external jet and ambient fluid (these are the external primary vortices). This means that there are no vortex pairings during this first transition step.

The three-dimensionalization turbulence is initiated only from $x/D_p = 15$, and in this region, the flow vortices no longer have a preferential direction. In this region, we observe the partial emergence of secondary vortices. There is also a sudden increase in turbulence at small eddies at the end of the domain, and the jet is in a fully developed state of turbulence.

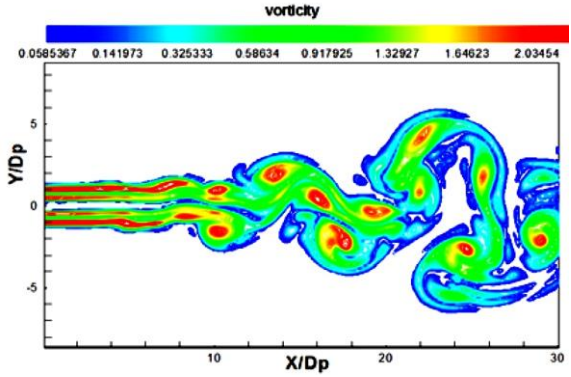

Fig. 7: Cut through the plane (x, y) of the vorticity field

Figure 8 provide the RMS velocity axial component profile as a function of transverse direction *y* in fully developed region.

The self-similarity state of the flow is obtained in this region, which indicates a good result of this simulation.

The RMS transverse velocity component profile for different axial positions is illustrated in figure 9. In addition, RMS profile at the beginning of the jet shows two distinct peaks located at the inner and outer sheared layers, respectively, the intensity of the two peaks is responsible for the turbulent mixing efficiency in the jet.

Close to the nozzle inlet, and due to the blocking phenomenon, the frequencies calculated from the signal of the RMS transverse velocity in each of the sheared layers are equal.

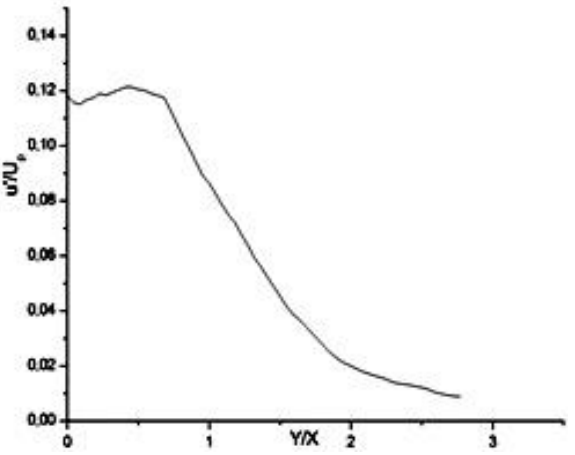

Fig. 8: RMS axial velocity profile

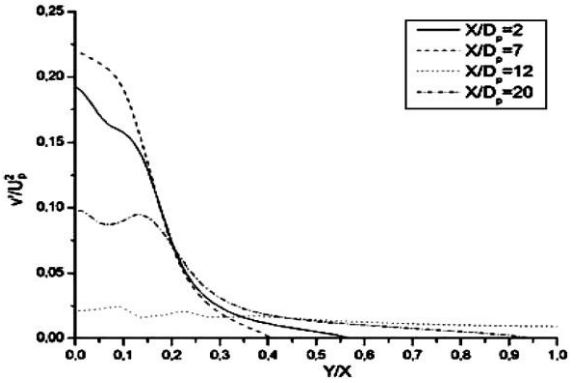

Fig. 9: RMS transverse velocity profile at different positions x/D_p

Figure 10 shows the Reynolds' tension $\overline{v'v'}$ profile. The latter confirms the presence of wake instability as soon as the nozzle jet exits. Reynolds tensions opposite direction of rotation. The expansion and interaction of these vortices with downstream distance is confirmed by the expansion and decrease of peaks in $\overline{v'v'}$ profile

The axial and transverse components evolution of Reynolds tensor is shown in figures 11 and 12. The axial Reynolds tensor contribution is associated with primary instability and primary vortices growth while transverse.

Reynolds tension contribution is associated with secondary instability which is at the origin of secondary vortices. The primary instability also dominates the evolution of secondary instability up to $x/D_p = 10$.

Figure 13 shows the turbulent kinetic energy distribution on transverse flow location in fully developed turbulence. The self-similarity state of the flow is obtained in this region, which indicates a good result of this simulation.

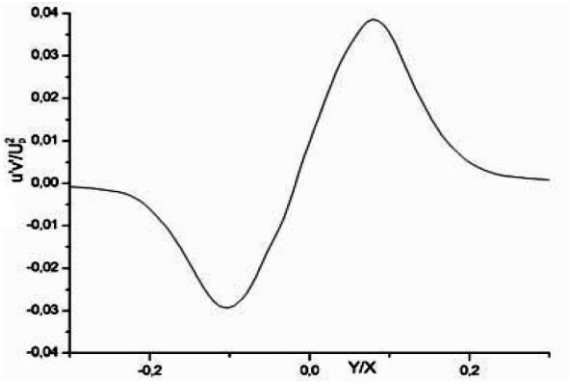

Fig. 10: Shear stress Reynolds `ν`ν

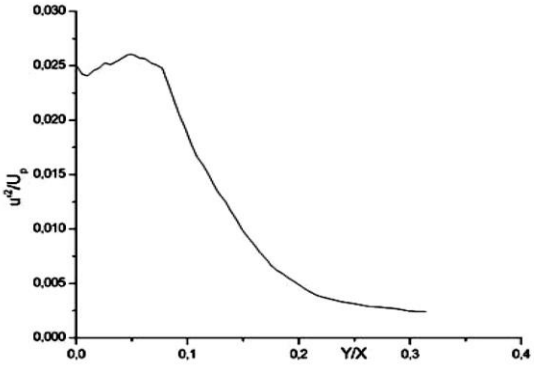

Fig. 11: Axial Reynolds tensor profile σ_{xx}

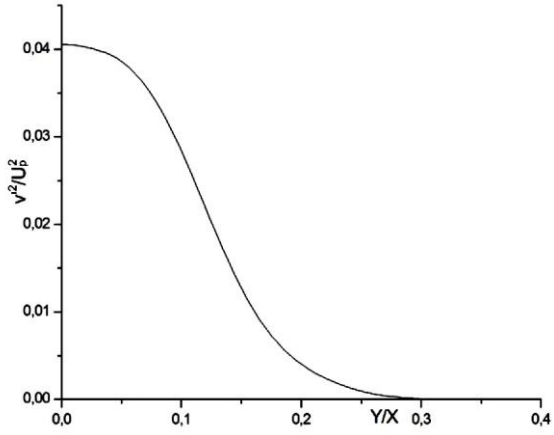

Fig. 12: Transverse Reynolds tensor profile σ_{yy}

The high transfer of momentum quantity from the primary jet to the secondary jet is due to longitudinal vortices. However, the level of turbulent intensity remains important during this jet width.

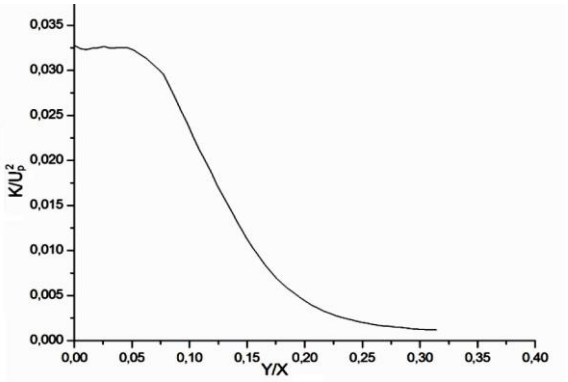

Fig. 13: Kinetic energy turbulent

The Power Spectral Density, 'PSD' of unsteady fields of radial velocity is shown in figure 14. Figure 14 gives PSD as a function of the number of Strouhal: $St = f\, U_p \,/\, D_p$, evaluated in the initial region of fully developed turbulence along with the $r = R_p$ and $r = R_s$

In $x/D_p = 4$, the predominance of an axis-symmetric mode on each of the shear layers is observed. This mode is characterized by Strouhal number peaks $St = 0.6$ in inner shear and $St = 0.7$ for the outer layer. This result is consistent with Bogey *and al.* [26] work.

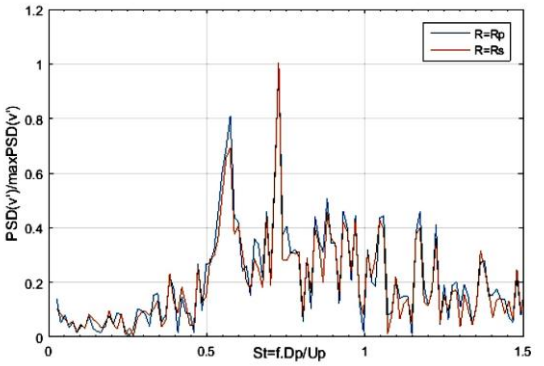

Fig.14: PSD radial velocity profile

Figures 15 and 16 represent the spectra development of longitudinal velocity fluctuations and the temperature on the primary jet axis at x/D_p=10 .

For the velocity case, the spectrum has an inertial zone with a power law in $K = -5/3$ over more than one decade followed by a dissipative region. This $-5/3$ slope is a good indication that, by that point, the flow has reached a fully developed turbulent state. This spectral behavior is interpreted as the result of vortex stretching by velocity gradients at large eddies.

In terms of temperature, the spectrum has a power law of $K = -1$. The temperature spectrum clearly validatesthe good behavior of the subgrid model used in this study.

These results confirm that coaxial jets can be assimilated to single jets in a fully developed area.

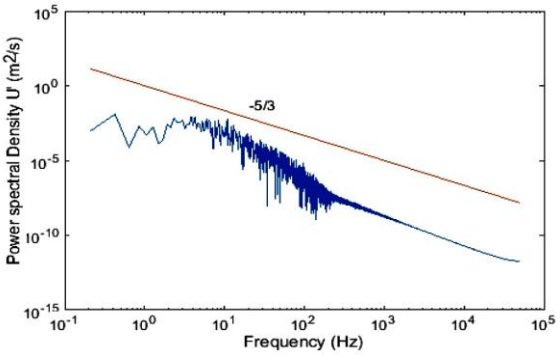

Fig. 15: PSD unsteady fields of axial velocity

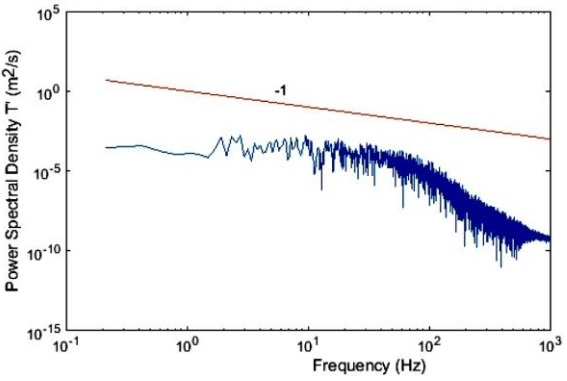

Fig. 16: PSD of temperature fields

5. CONCLUSION

This paper has presented a compressible turbulent coaxial jet using a numerical Large Eddy Simulation approach. This study is articulated on the implementation of a high-performance and modern numerical method to meet the requirements in terms of results accuracy and calculation cost. Therefore, this work aims to understand the transition process from laminar to turbulent flow of coaxial jet. White noise was overlaid at the laminar flow inlet to trigger jet disruption and development of Kelvin-Helmholtz eddies in shear layers. Different transition steps to fully developed turbulence of the coaxial jets were identified from a vortex point of view.

This transition was initiated by the development of Kelvin Helmholtz instabilities at shear layers. This instability resulted from vortices forming rings (primary vortices).

The second transition step initiated beyond $x/D_p = 15$, and the three-dimensional turbulence began to emerge with the appearance turbulence began to emerge with the appearance of secondary vortex segments (secondary vortices). The Reynolds tensors components transverse evolution showed that axial Reynolds tensor contribution was associated with primary instability and primary vortices growth while Reynolds transverse tension contribution was associated with secondary vortices.

The Reynolds tensors opposite to average velocity gradients indicated the presence of vortices structures having opposite directions of rotation. The expansion and

interaction of these vortices with axial direction flow was confirmed by jet width and peaks decrease in `v`v profile.

The self-similarity state of the flow is obtained in fully developed turbulence region. This result confirms the good quality of our experiments. The longitudinal velocity fluctuation development and temperature fluctuation spectra on jet axis at $x/D_p = 10$, for the velocity case, the spectrum has an inertial zone with a power law in $K = -5/3$ over more than one decade followed by a dissipative region.

This $-5/3$ slope is a good indication that, by that point, the flow has reached a fully developed turbulent state. A power law $k = 1$ was also noticed for spectrum temperature.

The temperature spectrum clearly validates the good behavior of the subgrid model used in this study.

The temporal power spectral density (PSD) of the radial velocity fluctuations as a function of the Strouhal number St evaluated in the initial fully developed turbulence region along the internal and external shear layer. Axisymmetric mode predominance on each of the shear layers (internal and external) has been observed.

NOMENCLATURE

θ_p , Momentum thickness of the primary jet	θ_s , Momentum thickness of the second. jet
B , Limiter flux	CFL , Courant-Friedrichs-Lewy
e , Interne energy	M , Mach number
F , Flux in x-direction	G , Flux in y-direction
H , Flux in z-direction	n , Number of time step
P , Pressure	Pr , Prandt number
Re , Reynolds number	Pr_{sgs} , Prandt number of subgrid scale
R_p , Inner radius of the coaxial jet	$R_{s\circ}$, Outer radius of the coaxial jet
R_m , Average radius of the coaxial jet	S_{ij} , Strain rate tensor
T , Temperature	T_p , Temperature of jet primary
T_∞ , Temperature of ambient air	u_i , Three velocity components
U_S , Velocity of the primary jet	U_P , Velocity of the secondary jet
x_i , Coordinate cartesien, x, y, z	U_∞ , Velocity of air ambient
t , Time	Δt , Time iteration method
VNN , Von Neumann number	$w[\rho, u, v, w, \rho]$, Primitives' variable
$U[\rho, \rho u, \rho v, \rho w, \rho e]$,	Filtered conserved vector
v_{sgs} , Turbulent eddy viscosity	τ_{ij} , SGS stress tensor
μ , Dynamical viscosity coefficient	μ , Kinematic viscosity molecular
ρ , Density	γ , Specific heat ratio
δ_{ij}, Kronecker symbol	Δ , Filter width of the LES filter
$minimod$, Minimod function	$(1 \pm 1/2)$, Interface volume control
(i, j) , Index of the three components	$\Delta x, \Delta y, \Delta z$, Grid size

REFERENCES

[1] F.H. Champagne, and I.J. Wygnanski, '*An experimental investigation of coaxial turbulent jets*', International Journal of Heat and Mass Transfer, Vol. 14, N°9, pp. 1445 - 1464, 1971.

[2] H.A. Warda, S.Z. Kassab, K.A. Elshorbagy, and E.A. Elsaadawy, '*An experimental investigation of the near-field region of a free turbulent coaxial jet using LDA*', Flow Measurement and Instrumentation, Vol. 10, pp. 15 - 26, 1999.

[3] W. Forstall, and A.H. Shapiro, '*Momentum and mass transfer in coaxial gas jets*', Journal of Applied Mechanics, Vol. 18 pp. 219 - 223, 1951.

[4] N.W.M. Ko, and A.S.H Kwan, '*The initial region of subsonic coaxial turbulent jets*', Journal of Fluid Mechanics, Vol. 73, Part 2, pp. 305 - 332, 1976.

[5] A.S.H. Kwan, and N.W.M. Ko, '*The initial region of subsonic coaxial jets*', Journal of Fluid Mechanics, Part 2, Vol. 82, pp. 273 - 287, 1977.

[6] G. Buresti, P. Petagna, and A. Talamelli, '*Experimental investigation on the turbulent near-field of coaxial jets*', Experimental Thermal Fluid Sciences, Vol. 17, pp. 18 - 26, 1998.

[7] C.S. Crow, and F.H. Champagne, '*Orderly structure in jet turbulence*', Journal of Fluid Mechanics, Vol. 48, pp. 547 - 591, 1971.

[8] E. Villermaux, and H. Rehab, '*Mixing in coaxial jets*', Journal of Fluid Mechanics, Vol. 425, pp. 161 - 185, 2000.

[9] H. Rehab, E. Villermaux, and E.J. Hopfinger, 'Flow regimes and mixing in the near field of large velocity ratio coaxial jets', 11th Symposium on Turbulent Shear Flows, Grenoble, France, 8-10 Septembre, Vol. 3, N°25, pp. 7 - 10, 1997.

[10] P.C. Ferrao, M. Heotor, M. Matos, and R.K. Salles, '*Turbulent scalar mixing in coaxial jet flows*', Proceedings of 1st International Conference on Turbulence and Shear Flows Phenomena, Santa Barbara, California, USA, 1990.

[11] C.B. Da Silva and O. Métais, '*Coherent structures in excited spatially evolving round jets*', Direct and Large-Eddy Simulation 4, pp. 205 - 212. New York Kluwer, 2001.

[12] C.B. Da Silva, G. Balarac, and O. Metais, '*Transition in high velocity ration coaxial jets analysed from direct numerical simulations*', Journal of Turbulence, Vol. 4, N°1, pp. 1 - 18, 2003.

[13] G. Balarac, and O. Metais, '*The near field of coaxial jets*', Physics of Fluids, Vol. 17, 065102, 2005.

[14] G. Balarac, M. Si-Ameur, M. Lesieur, and O. Metais, '*Direct numerical simulations of high velocity ratio coaxial jets: mixing properties and influence of upstream conditions*', Journal of Turbulence, Vol. 8, 1–14, 2007.

[15] M. Dianat, Z. Yang, D. Jiang, and J.J. Mcguirk, '*Large eddy simulation of scalar mixing in a coaxial confined jet Flow*', Turbulence Combustion, Vol. 77, pp. 205 - 227, 2006.

[16] S. Jahnke, N. Kornev, I. Tkatchenko, E. Hassel, and A. Leder, '*Numerical study of influence of different parameter on mixing in coaxial jet mixer using LES*', Heat Mass Transfer, Vol. 41, pp. 471 - 481, 2005.

[17] G. Balarac and M. Si-Ameur, '*Mixing and coherent vortices in turbulent coaxial jets*', Comptes Rendus Mécanique, Vol. 333, N°8, pp. 622 - 627, 2005.

[18] K.K.J.R. Dinesh, A.M. Savill, K.W. Jenkins, M.P. Kirkpatrick, '*A study of mixing and intermittency in a coaxial turbulent jet*', Fluid Dynamics Research, Vol. 42, N°2, pp. 1 - 20, 2010.

[19] R.G. Michael, '*Numerical investigation on hydrodynamic and noise radiation of coaxial jets flows*', Thesis Doctor of Sciences of ETH Zurich, 2014.

[20] J. Smagorinsky, '*General circulation experiments with the primitive equations*', Monthly Weather Review, Vol. 91, N°3, pp. 99 - 164, 1963.

[21] C.B. Laney, '*Computational Gas Dynamics*', Cambridge University Press, 1993.

[22] V.I. Kopchenov, and A.N. Kraiko, '*A monotonic second-order difference scheme for hyperbolic systems with two independent variables*', U.S.S.R. Computational Mathematics and Mathematical Physics, Vol. 23, N°4, pp. 50 - 56, 1983.

[23] S. Yamamoto, and H. Daiguji, '*Higher order accurate upwind schemes for solving compressible Euler and Navier–Stokes equations*'. Computers &. Fluids, Vol. 22, N°2/3, pp. 259 - 270, 1993.

[24] R.W. MacCormack, '*The Effect of Viscosity in Hyper Velocity Impact Cratering*', Journal of Space Craft, pp. 9 - 354, 1969.

[25] A. Guitton, *Etude expérimentale des relations entre les champs hydrodynamiques et acoustiques des jets libres*. Thèse de Doctorat. Université de Poitiers, 2009.

[26] C. Bogey, C. Barre, P. Juve, and C. Bailly, '*Simulation of a hot coaxial jet: Direct noise prediction and flow-acoustics correlations*', Physics of Fluids, Vol. 21, N°3, 2009.